



## Full length article

# Photo-induced disinfection property and photocatalytic activity based on the synergistic catalytic technique of Ag doped TiO<sub>2</sub> nanofibers

Ming-Chung Wu<sup>a,b,c,\*</sup>, Ting-Han Lin<sup>a</sup>, Kai-Hsiang Hsu<sup>c,d</sup>, Jen-Fu Hsu<sup>c,e,\*</sup>

<sup>a</sup> Department of Chemical and Materials Engineering, College of Engineering, Chang Gung University, Taoyuan 33302, Taiwan

<sup>b</sup> Green Technology Research Center, Chang Gung University, Taoyuan 33302, Taiwan

<sup>c</sup> Division of Pediatric Neonatology, Department of Pediatrics, Chang Gung Memorial Hospital, Linkou, Taoyuan 33305, Taiwan

<sup>d</sup> Graduate Institute of Clinical Medical Science, Chang Gung University, Taoyuan 33302, Taiwan

<sup>e</sup> School of Traditional Chinese Medicine, College of Medicine, Chang Gung University, Taoyuan 33302, Taiwan



## ARTICLE INFO

## Keywords:

Photocatalyst

Silver doped

TiO<sub>2</sub>

Photodegradation

Disinfect bacteria

## ABSTRACT

Various metal-doped TiO<sub>2</sub> nanofibers were prepared by hydrothermal synthesis followed by the thermal treatment in air. An array of metal dopants including Ag, Au, Co, Cr, Cu, Fe, Ni, Pd, Pt, Y, and Zn, were respectively doped into TiO<sub>2</sub> NFs to acquire the visible-light photocatalytic activity. Considering the photodegradation results under visible-light illumination, Ag doped TiO<sub>2</sub> NFs was chosen to study further. Then, the optimal doping level and calcination process were studied systemically to obtain the highly visible light active Ag doped TiO<sub>2</sub> NFs. As the Ag doping concentration increased up to 5.00 mol%, anatase to rutile phase transition was observed. Meanwhile, based on the consistent results of synchrotron X-ray spectra, element analysis, and morphological observation, Ag<sub>2</sub>O was detected and located on the surface of as-synthesized Ag doped TiO<sub>2</sub> NFs. Thus, the photodegradation of methyl orange by using 5.00 mol%-Ag doped TiO<sub>2</sub> NFs calcined at 600 °C performed the highest visible-light photodegradation activity. Moreover, it also showed the excellent disinfection against *E. coli* and *S. aureus* under visible light due to the synergistic effect of Ag<sub>2</sub>O and photo-induced reactive oxygen species (ROS) formed by TiO<sub>2</sub> photocatalyst. The synthesized Ag doped TiO<sub>2</sub> NFs makes large-scale and convenient fabrication possible, and it has tremendous practical potentials in the photodegradation of environmental pollution and disinfects bacteria behavior.

## 1. Introduction

Titanium dioxide (TiO<sub>2</sub>) photocatalytic phenomena attract a lot of interests due to its ability to destroy organic compounds in contaminated air or water [1–4] and its antibacterial behavior [5–7]. TiO<sub>2</sub> shows many advantages, such as low cost, environmentally friendly, non-toxic to human, and high photocatalytic activity. However, its practical applications are greatly restricted due to the wide band gap (anatase TiO<sub>2</sub> ~ 3.2 eV; rutile TiO<sub>2</sub> ~ 3.0 eV) and low separation probability of the photoinduced electron-hole pairs [8–10]. Hence, numerous research groups have provided a lot of ways to enhance absorbing ability in the visible range. The one-dimensional titanate materials synthesized from TiO<sub>2</sub> powders in alkaline solutions have opened up new possibilities for large-scale and simple production of TiO<sub>2</sub> nanofibers by annealing the obtained titanate materials in the air. In the practical applications, one-dimensional materials are much easier to achieve a percolated electrical network with elongated materials than ordinary nanoparticles [11–13]. Furthermore, bundling of one-

dimensional materials contributes some mechanical robustness in tangled networks and results in better entanglement with other nanofibers when forming macroscopic films [14–16].

In recent years, many efforts have been carried out to narrow the band gap. One of such efforts is to dope metal or non-metal onto TiO<sub>2</sub>. TiO<sub>2</sub> incorporated with non-metal element such as carbon [17–19], nitrogen [17,20–22], sulfur [23,24], fluoride [25,26], iodine [27,28], phosphor [29], and boron [30,31], have successfully narrowed the band gap and have extended absorption band over the visible region [32,33]. However, the photocatalytic activity is still not ideal. However, metal-doped TiO<sub>2</sub> with Au [34–36], Ag [37], Cu [38,39], Co [40], Fe [41,42], Pt [35,43,44], Pd [35,45,46], Ru [47], V [48], and Zn [49,50] have efficiently improved the separation of the electron and hole, and have reduced the recombination of electron-hole pair, which caused a substantial increase in photocatalytic activity. [51] Ag doped TiO<sub>2</sub> has been synthesized by sol-gel method, impregnated method, or hydrothermal method. The incorporation of silver ion increased the absorption band to the visible range and this promoted the

\* Corresponding authors at: Chang Gung University, Taoyuan 33302, Taiwan.

E-mail addresses: [mingchungwu@cgu.edu.tw](mailto:mingchungwu@cgu.edu.tw) (M.-C. Wu), [hsujanfu@cgmh.org.tw](mailto:hsujanfu@cgmh.org.tw) (J.-F. Hsu).

<https://doi.org/10.1016/j.apsusc.2019.04.028>

Received 23 November 2018; Received in revised form 30 March 2019; Accepted 2 April 2019

Available online 09 April 2019

0169-4332/ © 2019 Published by Elsevier B.V.

photocatalytic activity due to surface plasmon resonance [52–55]. These results show that incorporating metals onto TiO<sub>2</sub> significantly enhance the photocatalytic performance. The photocatalytic performance of metal doped TiO<sub>2</sub> depends on the concentration and the character of the dopant ion.

Metal oxides as photocatalyst have already adopted in antibiotic applications for killing bacteria, such as *Escherichia coli* (*E. coli*), *Staphylococcus aureus* (*S. aureus*), *Pseudomonas aeruginosa* (*P. aeruginosa*), and *Salmonella enterica* (*S. typhi*), and created a great knowledge base on kinetic mechanism of photocatalytic antibacterial [56–58]. The nanostructured TiO<sub>2</sub> doped with these photocatalysts, such as ZnO, CeO<sub>2</sub>, and Fe<sub>2</sub>O<sub>3</sub>, can produce large amounts of reactive oxygen species (ROS) including hydroxyl radical (<sup>•</sup>OH), singlet oxygen (<sup>1</sup>O<sub>2</sub>), and superoxide anion (O<sub>2</sub><sup>•-</sup>) to perform an outstanding antibiotic behavior under irradiation [57]. Considering the extension of visible-light absorption, using nanostructured TiO<sub>2</sub> that are single element doped, multi elements doped, or co-coated are the beneficial strategies in improving the activity both in the photodegradation of dye and in the antibiotic property [59–61]. Silver, the most appealing element in antibiotics, and its derivative compounds can be incorporated into TiO<sub>2</sub> nanomaterials to create a lot of potential. In case of relevant mechanism on the antibiotic property, the various heterojunctions in TiO<sub>2</sub> might directly contribute to the microstructure, the morphology, the chemical reaction path, and the reduction potential toward the formation of ROS. The comprehensive mechanism that depends on these factors should be investigated case by case in detail.

In this study, we first synthesized many kinds of metal doped TiO<sub>2</sub> NFs in searching for the optimal metal dopant, the optimal doping concentration, and the optimal calcination process. After comparing the visible-light photocatalytic activities and the cost of the metal precursor, Ag doped TiO<sub>2</sub> NFs showed that silver ion dopants are the best candidates. Aiming to optimize the photocatalytic activity of this series of nanofibers, the particle size, the optical properties, the crystal structure which was affected by calcination temperature, and doping concentration are further discussed. Furthermore, loading of Ag<sub>2</sub>O nanoparticles onto TiO<sub>2</sub> surface and the related chemical states were performed and further characterized. Finally, we presented their disinfection properties and the possible mechanism by analyzing the ROS.

## 2. Experimental details

For the synthesis of metal doped TiO<sub>2</sub> NFs, we added 2.50 g TiO<sub>2</sub> anatase powder (Aldrich, 98%) and various transition metal precursor into 62.5 mL of 10.0 M NaOH solution in a teflon-lined autoclave under 150 °C for 24 h. The transition metal precursors include: silver nitrate (AgNO<sub>3</sub>, CHONEYE), tetrachloroauric(III) acid trihydrate (HAuCl<sub>4</sub>·3H<sub>2</sub>O, ACROS), cobalt (II) nitrate hexahydrate (Co(NO<sub>3</sub>)<sub>2</sub>·6H<sub>2</sub>O, ACROS, 99%), chromium(III) nitrate nonahydrate (Cr(NO<sub>3</sub>)<sub>3</sub>·9H<sub>2</sub>O, ACROS, 99%), copper(II) nitrate trihydrate (Cu(NO<sub>3</sub>)<sub>2</sub>·3H<sub>2</sub>O, ACROS, 99%), Iron(III) nitrate nonahydrate (Fe(NO<sub>3</sub>)<sub>3</sub>·9H<sub>2</sub>O, ACROS, 98 + %), nickel (II) nitrate hexahydrate (Ni(NO<sub>3</sub>)<sub>2</sub>·6H<sub>2</sub>O, ACROS, 99%), yttrium(III) nitrate hexahydrate (Y(NO<sub>3</sub>)<sub>3</sub>·6H<sub>2</sub>O, ACROS, 99.9%), zinc nitrate hexahydrate (Zn(NO<sub>3</sub>)<sub>2</sub>·6H<sub>2</sub>O, CHONEYE, 97%). The doping concentration for all transition metal-doped TiO<sub>2</sub> was fixed at 1.00 mol%. In order to exchange sodium ion for proton, the metal doped sodium titanate nanofibers were washed with 0.10 M hydrochloric acid (HCl). After that, the products were washed in deionized water to be neutralized. After filtering, they were dried at 80 °C. Finally, metal doped TiO<sub>2</sub> NFs were calcined at 500, 550, 600, 650, and 700 °C, for 12 h with a heating rate of 5 °C/min.

In addition, UV–vis reflectance spectra of the various metal doped TiO<sub>2</sub> NFs were measured by UV-VIS Spectrophotometer (JASCO Analytical Instruments, V-650, Japan) in the 300–800 nm wavelength range. The crystal structures of the various metal doped TiO<sub>2</sub> NFs were determined by X-ray diffractometer (XRD, Bruker, D2 phaser with

Xflash 430) using Cu K<sub>α</sub> radiation at 30.0 kV and 300.0 mA. XRD patterns were collected from 2θ between 10 and 80 with a 0.005° step at 5° min<sup>-1</sup>. For Raman scattering spectra, the samples were positioned on a high-resolution piezoelectric stage of the scanning microscopy (WiTec, Alpha 300S) and were excited by a 532 nm He-Ne laser (25 mW). The laser beam was focused with a 10 × objective lens (Nikon plane objective, NA ≈ 0.9), and the diameter of the focused laser beam was about 10 μm. Spherical-aberration Corrected Field Emission Transmission Electron Microscope (JEOL, JEM-ARM200FTH, Japan) was used to observe the microstructures of Ag doped TiO<sub>2</sub>.

For the measurement of photodegradation activity, 20.0 mg of catalyst was sonicated for 1 min in 150 mL of 1.0 mg/L methyl orange (ACROS, pure) aqueous solution. The suspensions were left to relax for 30 min in order to minimize the error of the dye concentration measurements caused by initial surface adsorption. The temperature of the mixture was kept near room temperature. The light sources include UV-B lamps (Sankyo Denki G15T8E 8W, the wavelength of maximum emission is ~312 nm), and visible lamps (Goodly, F8T5/D 8W). The suspension under vigorous stirring was irradiated with the two lamps at ambient conditions. The distance between each lamp and reactor is about 5.0 cm. After centrifuging for 15 min at 5000 rpm, the absorption spectrum of the retained methyl orange and its derivatives in the supernatant was recorded by absorption spectrophotometer (JASCO Analytical Instruments, V-730, Japan) in the 300–800 nm wavelength range.

For the testing of disinfection, a gram-positive bacterium, *Staphylococcus aureus* (*S. aureus*, ATCC 25923), and a gram-negative bacterium, *Escherichia coli* (*E. coli*, ATCC 2952) were used as test bacteria. These two bacteria are both common pathogens in clinical practice. All of phosphate-buffered saline (PBS) solution and vessel were sterilized in autoclave at 125 °C for 30 min. Before mixing with TiO<sub>2</sub> suspension, *S. aureus* and *E. coli* were activated respectively and further suspended in PBS solution in a diluted concentration of ~10<sup>6</sup> CFU/mL. On the other hand, 10.5 mg of various TiO<sub>2</sub> including pristine TiO<sub>2</sub> NFs, AEROXIDE® P25 TiO<sub>2</sub> (TiO<sub>2</sub>-P25), and Ag doped TiO<sub>2</sub> NFs were dispersed well in 7.0 ml of deionized water, respectively. Next, 1.0 mL of TiO<sub>2</sub> suspension and 5.0 ml of bacterial suspension were mixed in an optical glass tube. These tubes were placed under 2 pieces of visible light lamp (Goodly, F8T5/D, 8W). The distance between lamp and tube was consistently at 10 cm. The mixtures were incubated at 37 °C for 24 h under visible irradiation. At various irradiation intervals, the mixtures were sampled and re-cultivated on agar plate at 37 °C for 24 h to observe the growth behavior of bacterial colonies.

## 3. Results and discussion

### 3.1. Photodegradation of various transition metal doped TiO<sub>2</sub> nanofibers

Transition metal doping has been considered an efficient strategy in the TiO<sub>2</sub> modification. The eleven kinds of transition metal dopants including Ag, Au, Co, Cr, Cu, Fe, Ni, Pd, Pt, Y, and Zn were doped into TiO<sub>2</sub> nanofibers by hydrothermal synthesis and further calcined at 600 °C in air. To evaluate the photocatalytic activity, these various TiO<sub>2</sub> NFs were firstly tested in the degradation of methyl orange (Fig. 1). Specific metal dopants including Cu, Pd, Pt, Zn, and Ag presented the excellent photodegradation activity under UV irradiation. Compared to pristine TiO<sub>2</sub> and commercial TiO<sub>2</sub>-P25, the as-mentioned dopants also showed higher photocatalytic activity. The slightly doping concentration in the TiO<sub>2</sub> photocatalyst usually enhances the optical absorption as well as increases the conductivity and/or improves their crystallinity to promote the charge carrier transport. However, in the case of chromium as dopant, it showed quite low photocatalytic activity. It might be attributed that the excessed Cr dopant in the TiO<sub>2</sub> might directly destroy the crystallinity of TiO<sub>2</sub> NFs and further reduce their activity. Among them, Ag doped TiO<sub>2</sub> showed the highest activity under UV irradiation. For the practical application, the visible-driven

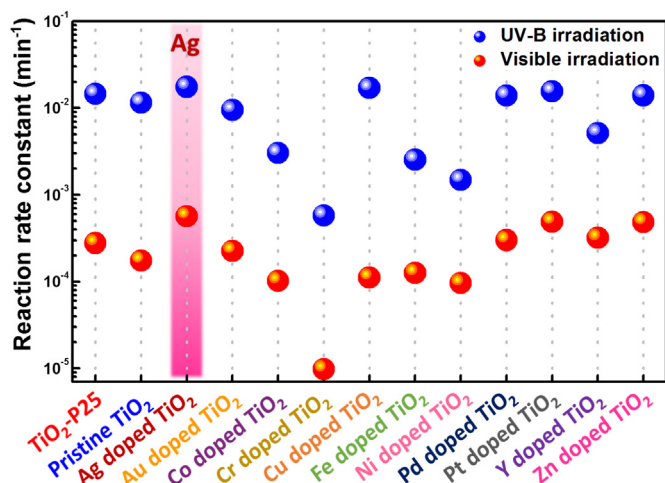


Fig. 1. The photodegradation activity of TiO<sub>2</sub> P25, pristine TiO<sub>2</sub>, and various transient metal doped TiO<sub>2</sub> NFs under UV-B irradiation and visible light irradiation.

photocatalysis and competitive price must be considered. Among these metal dopants, the photocatalytic activity of Y dopant has been promoted due to the improved optical absorption. Particularly, Pd, Pt, Zn, and Ag still maintained excellent photodegradation behavior. In this case, Ag dopant not only shows the highest activity under visible illumination, but Ag dopant is also at the acceptable cost compared to Pd and Pt. Meanwhile, silver derivatives reveal the cytotoxicity and possess an excellent potential on the water disinfection. Thus, Ag was chosen for further investigation.

### 3.2. Optimizing annealing condition of Ag doped TiO<sub>2</sub> nanofibers

The annealing process usually dominates various crystal structures and crystallinity, further presenting various photocatalytic performance. In order to find the optimal preparation process, we calcined Ag doped TiO<sub>2</sub> at various temperatures in air for 12 h. These samples were denoted as Ag doped TiO<sub>2</sub>-X where the symbol “X” represents the calcination temperature. The crystal structures of the Ag doped TiO<sub>2</sub>-X series were characterized by X-ray diffractometer as shown in Fig. S1(a). The intensity of reflection for Ag doped TiO<sub>2</sub>-X series increased as calcination temperature increased because the rising calcination

temperature improved the ordering of anatase TiO<sub>2</sub> lattice. At the calcination temperature of 650 °C, the diffraction peaks of Ag doped TiO<sub>2</sub>-650 can be perfectly indexed as the body-centered tetragonal unit cell of anatase TiO<sub>2</sub>, with unit cell parameters  $a = b = 3.78 \text{ \AA}$  and  $c = 9.52 \text{ \AA}$  [JCPDS 21-1272]. The crystallite size of (101) plane in anatase TiO<sub>2</sub> is estimated by using Debye-Scherrer equation to discover the calcination temperature effect on the crystal structure.

The mean crystalline domain sizes are calculated by Debye-Scherrer equation.

$$\tau = \frac{K\lambda}{\beta \cos\theta} \quad (1)$$

Here,  $\tau$  is the mean size of the crystalline;  $K$  is a dimensionless shape factor of 0.9;  $\lambda$  is the CuK $\alpha$  wavelength of 1.54 Å;  $\beta$  represents the full width at half maximum; and  $\theta$  is the angle of the diffraction peak. As shown in Fig. S1(b), increasing the calcination temperature leads to the formation of large crystallite size. In this case, few silver dopant existed in TiO<sub>2</sub> lattice did not lower the ordering arrangement and exhibited a similar tendency compared to pristine TiO<sub>2</sub> nanofibers [62].

The Ag doped TiO<sub>2</sub>-X series was further investigated by photodegradation of methyl orange as shown in Fig. S1(c). The photodegradation of methyl orange mostly follows Langmuir-Hinshelwood kinetics, which can be simplified to the first-order kinetics at lower initial methyl orange concentrations, mathematically described as  $-\ln(C/C_0) = kt$ , where  $C$  is the concentration of methyl orange at time  $t$ ,  $C_0$  is the initial concentration of methyl orange, and  $k$  is the apparent reaction rate constant [63,64]. Plotting the logarithm of the reciprocal of methyl orange concentrations as a function of time can further obtain the linear slopes as the reaction rate constant  $k$  for various Ag doped TiO<sub>2</sub>-X. Ag doped TiO<sub>2</sub>-600 showed the highest reaction rate constant among the Ag doped TiO<sub>2</sub>-X series. Its calculated rate constant was  $\sim 0.021 \text{ min}^{-1}$  (Fig. S1(d)). Thus, we chose Ag doped TiO<sub>2</sub>-600 for the further study.

### 3.3. Optimizing doping level on Ag doped TiO<sub>2</sub> nanofibers

The correlation between doping concentration and crystal structure of Ag doped TiO<sub>2</sub>-600 series with various doping levels were studied. These Ag doped TiO<sub>2</sub>-600 were denoted as Y-Ag doped TiO<sub>2</sub> where the symbol “Y” represents the doping levels. Raman spectra of Y-Ag doped TiO<sub>2</sub> series can be clearly assigned to the typical phonon vibration mode of anatase TiO<sub>2</sub>, which are illustrated as shown in Fig. S2. But, the weak Raman scattering signal of silver was not detectable even when

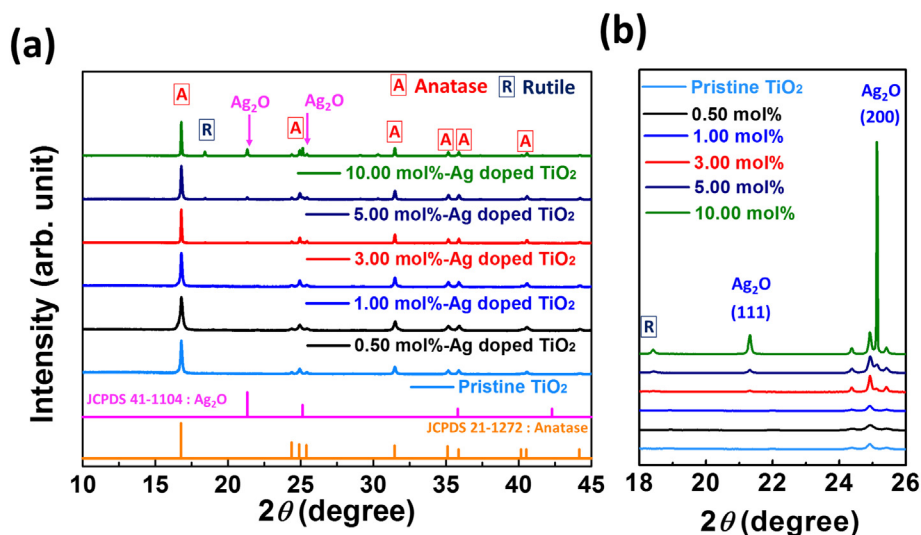


Fig. 2. (a) Synchrotron X-ray spectra and (b) the magnified synchrotron X-ray spectra at  $2\theta$  ranged from 18.0 to 26.0° of Y-Ag doped TiO<sub>2</sub> series with slow scan rate of  $0.005^\circ \text{ s}^{-1}$ .

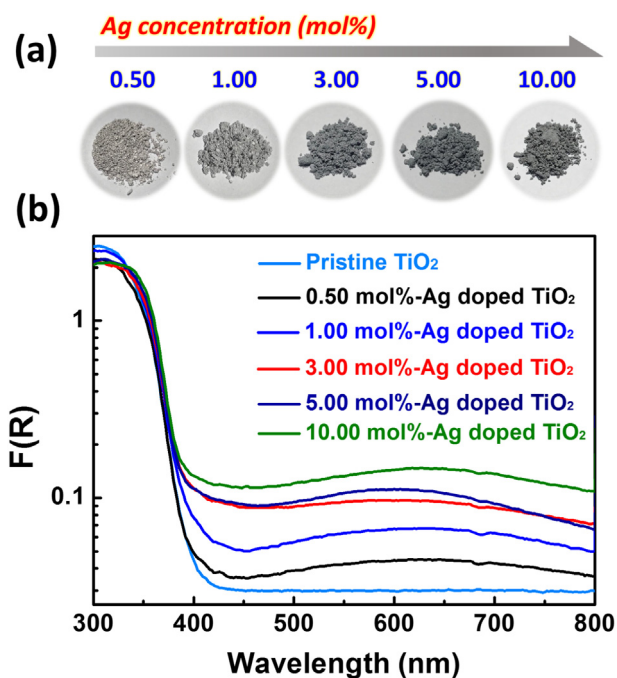


Fig. 3. (a) Appearance and (b) Kubelka–Munk function spectra of Y-Ag doped  $\text{TiO}_2$  series.

the doping concentration reached 10.00 mol%. For intense study of silver characterization, we studied the crystal structure by measuring the relevant synchrotron X-ray spectroscopy. In Fig. 2, we found that all diffraction peaks are derived from  $\text{TiO}_2$  anatase phase as the doping concentration ranged from 0.00 to 3.00 mol%. Interestingly, when the Ag doping level reached above 5.00 mol%, the diffraction of  $\text{Ag}_2\text{O}$  and  $\text{TiO}_2$  rutile phase were both present. It meant that the increased doping concentration might cause  $\text{TiO}_2$  phase transformation from anatase to rutile because the ordering arrangement of anatase phase was reduced by silver dopant. Meanwhile,  $\text{Ag}_2\text{O}$  might start to precipitate and exist in the  $\text{TiO}_2$  structure. The diffraction peak can be respectively indexed to (111) plane and (200) plane of  $\text{Ag}_2\text{O}$  at  $2\theta$  of  $21.32^\circ$  and  $25.13^\circ$  [JCPDS 41-1104].

The Ag doping effect on  $\text{TiO}_2$  contributes to the difference of optical properties. The appearances of various  $\text{TiO}_2$  catalysts are shown in Fig. 3(a) and their color darkened as the doping level increased. To understand the relationship between Ag doping levels and optical properties, the Kubelka–Munk function was used to measure as shown in Fig. 3(b). We can observe that the absorbance in visible light increases as the Ag doping concentration increases, which can be attributed to the typical absorption of  $\text{Ag}_2\text{O}$  and surface plasmon resonance by Ag depositing on  $\text{TiO}_2$  surface.

Y-Ag doped  $\text{TiO}_2$  series was further investigated for the photodegradation of methyl orange (Fig. 4(a)). Under 16 W of visible light irradiation, 5.00 mol%-Ag doped  $\text{TiO}_2$  gave the fastest decoloration phenomenon for the photodegradation of methyl orange. Its calculated rate constant was  $\sim 1.4 \times 10^{-3} \text{ min}^{-1}$ . In case of visible light irradiation, the entire Y-Ag doped  $\text{TiO}_2$  series showed higher activity than commercial  $\text{TiO}_2$ -P25 due to the significant optical absorption. In the meantime, 5.00 mol%-Ag doped  $\text{TiO}_2$  showed stronger photodegradation activity to rhodamine 6G and brilliant green (Fig. 4(b)) owing to the significant adsorption behavior. It is attributed that two cationic dyes are easily attracted by photo-induced electrons on Ag doped  $\text{TiO}_2$ . The related specific surface area measured by BET and BJH method were reported in Table S1. Compared to pristine  $\text{TiO}_2$  NFs, 5.00 mol%-Ag doped  $\text{TiO}_2$  showed higher surface area. We speculated that there were different morphologies constructed in nanoscopic. Besides, the photocatalyst revealed a good stability as shown in Fig. S3. The

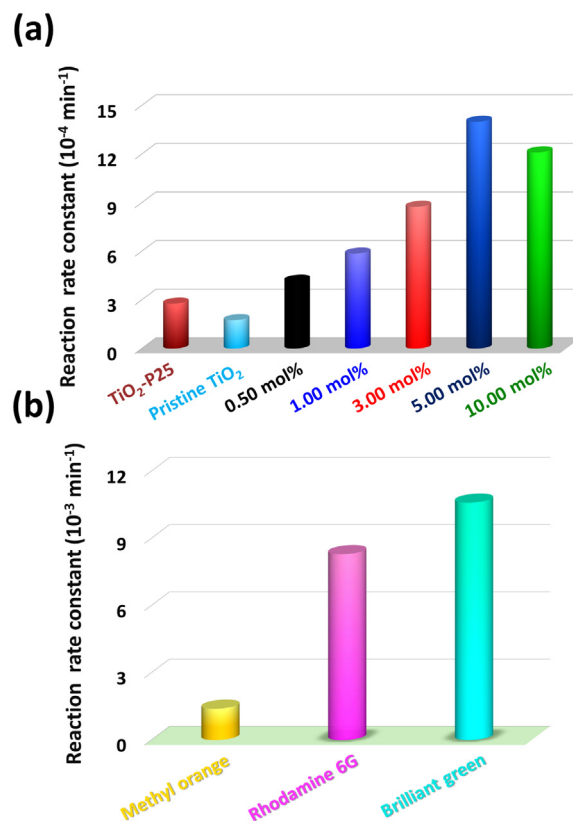


Fig. 4. The bar graph of photodegradation reaction rate constants of (a)  $\text{TiO}_2$ -P25, pristine  $\text{TiO}_2$ , and Y-Ag doped  $\text{TiO}_2$  series under visible light irradiation, and (b) 5.00 mol%-Ag doped  $\text{TiO}_2$  toward methyl orange, rhodamine 6G, and brilliant green.

degradation activity can be maintained after stored at ambient condition for 6 months. After used in the photodegradation experiment, we found that the intensity of diffraction peak at  $2\theta$  of  $25.3^\circ$  did not decrease (Fig. S4). It was attributed to the chemical state of silver oxide was stable and did not to form other silver derivatives. These results provided the additional evidence to explain the superiority of Ag doped  $\text{TiO}_2$  on the application of the photodegradation.

The microstructures of 5.00 mol%-Ag doped  $\text{TiO}_2$  was observed by HRTEM. For Fig. 5(a), we can observe that  $\text{TiO}_2$  is present as nanofiber. Moreover, we found that some nanoparticles deposited on the surface of 5.00 mol%-Ag doped  $\text{TiO}_2$  (Fig. 5(b)) and its particle size is  $\sim 10 \text{ nm}$  (Fig. 5(c)). It is clear evidence to depict the higher surface area of Ag doped  $\text{TiO}_2$ . The  $d_{101}$  of anatase phase in the Ag doped  $\text{TiO}_2$  is about  $3.53 \text{ \AA}$ , (Fig. S5(a)) while  $d_{200}$  of silver oxide is about  $2.28 \text{ \AA}$ . (Fig. S5(b)) To further confirm the chemical composition of nanoparticles deposited on the surface of  $\text{TiO}_2$ , the energy dispersive X-ray analysis was applied in this study. Fig. 5(d) shows the chemical distribution of each components, including silver (Fig. 5(e)), oxygen (Fig. 5(f)), and titanium (Fig. 5(g)). From the results of energy dispersive X-ray analysis, the nanoparticles deposited on the surface of 5.00 mol%-Ag doped  $\text{TiO}_2$  is silver oxide.

To clarify the exact loading of silver and silver oxide in the Ag-doped  $\text{TiO}_2$ , we further studied the surface composition by XPS as shown in Fig. S6 and Table 1. With increasing the doping concentration, Ag molar ratio of Y-Ag doped  $\text{TiO}_2$  series was increased and showed a higher concentration than theoretical doping concentration. It can be attributed to most of the silver/silver oxide that existed near the  $\text{TiO}_2$  surface. The other related elements including Ti and O were presented in Figs. S7 and S8. Furthermore, the respective loading amount of Ag,  $\text{Ag}_2\text{O}$ , and AgO were calculated as listed in Table S2. Few amounts of metallic Ag and AgO compound can be identified. Over half of the

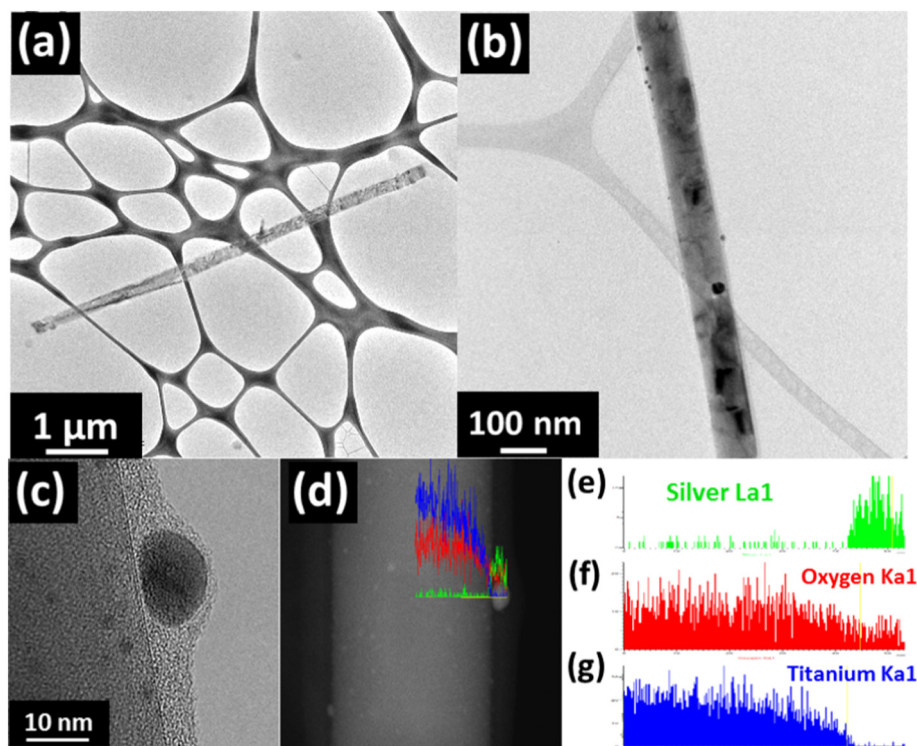


Fig. 5. (a,b) HRTEM images, (c) high-magnification image, (d) energy dispersive X-ray spectra, and chemical component distribution of (e) silver, (f) oxygen, and (g) titanium, of 5.00 mol%-Ag doped TiO<sub>2</sub>.

Table 1

Ag molar ratio of Y-Ag doped TiO<sub>2</sub> series.

Sample	Ag / Ti + Ag (%)
0.50-Ag doped TiO <sub>2</sub>	3.1
1.00-Ag doped TiO <sub>2</sub>	7.2
3.00-Ag doped TiO <sub>2</sub>	12.8
5.00-Ag doped TiO <sub>2</sub>	16.6
10.00-Ag doped TiO <sub>2</sub>	16.6

loading amounts was dominated by Ag<sub>2</sub>O. According to the above results and analysis of synchrotron X-ray spectroscopy, we clarified that Ag<sub>2</sub>O nanocomposite is mainly consisted in the Ag doped TiO<sub>2</sub>.

### 3.4. Disinfection properties of Ag doped TiO<sub>2</sub> nanofibers

The disinfection of the Ag doped TiO<sub>2</sub> NFs under visible light irradiation was investigated. The bacterial colonies of *S. aureus* and *E. coli* are shown in Figs. 6 and S9. Compared to the control experiment, we clearly observed that the colonies of *S. aureus* incubating with TiO<sub>2</sub>-P25 and pristine TiO<sub>2</sub> kept in high density as incubation time increased. The growth of *S. aureus* was not affected by either TiO<sub>2</sub>-P25 or pristine TiO<sub>2</sub>, and survived well in PBS/TiO<sub>2</sub> solution at all time. Also, it could be explained that the photocatalytic activities of both TiO<sub>2</sub>-P25 and pristine TiO<sub>2</sub> were quite low under visible irradiation. There was not enough ROS against *S. aureus*. In contrast, when *S. aureus* was incubated with 5.00 mol%-Ag doped TiO<sub>2</sub> in PBS solution, the bacterial colonies decreased rapidly since the first hour, and the colony did not expand as the incubation time increased. This growth inhibition was even more obvious in *E. coli* disinfection experiment (Fig. S9). We found that the colonies of *E. coli* vanished earlier than that of *S. aureus*. The finding may be related to the thinner peptidoglycan layer of the *E. coli* membrane. Based on the above results, we proposed that there was a synergistic effect by Ag doped TiO<sub>2</sub> against bacteria, which attributed to ROS being produced by TiO<sub>2</sub> and Ag ions. These radicals could damage

the cellular membrane and cause osmotic pressure imbalance, which resulted in bactericidal effect. Moreover, Ag ions or Ag nanoparticles usually play an important role in antibacterial activity. When Ag ions or Ag NPs from the Ag doped TiO<sub>2</sub> surface was slightly released or gotten close to bacteria, these Ag derivatives might react with cell membrane and alter its structure and permeability. These Ag ions or ROS produced by TiO<sub>2</sub> passed through damaged cell membrane easily and further oxidized the proteins. Several literatures also reported that Ag likely reacted with thiol group in proteins of bacteria [65–68]. Overall, Ag doped TiO<sub>2</sub> showed the most effective disinfect bacteria efficacy.

### 3.5. Possible disinfection mechanism

The ROS detection helps us realize the photocatalytic mechanism on the disinfection. Due to the similar reaction pathway between photodegradation and photo-induced disinfection, the detection of ROS can be performed directly in the way of a decoloration experiment of organic dyes with specific scavengers. We adopted three types of scavengers, including 1,4-benzoquinone (BQ), tert-butanol (TBA), and ammonia oxalate (AO) to investigate the formation of superoxide radicals, hydroxide radicals, and holes, respectively. In Fig. 7(a), during photodegradation of methyl orange by pristine TiO<sub>2</sub>, adding BQ significantly hindered the decoloration, while the AO and TBA only did slightly. In addition, we calculated the degradation efficiency of photodegradation, which is defined by:

$$\text{Degradation efficiency (\%)} = \left(1 - \frac{C_t}{C_i}\right) \times 100\% \quad (2)$$

where  $C_t$  and  $C_i$  respectively represent the terminal concentration and initial concentration of methyl orange in the photodegradation experiment. The calculated degradation efficiency for pristine TiO<sub>2</sub> without any scavengers is about 80% as shown in Fig. 7(c). Once BQ, TBA, and AO were respectively added to the photodegradation experiment, the degradation efficiencies obviously declined. It meant that there were lots of  $\cdot\text{OH}$  radicals, a few  $\text{O}_2\cdot^-$  radicals and holes formed

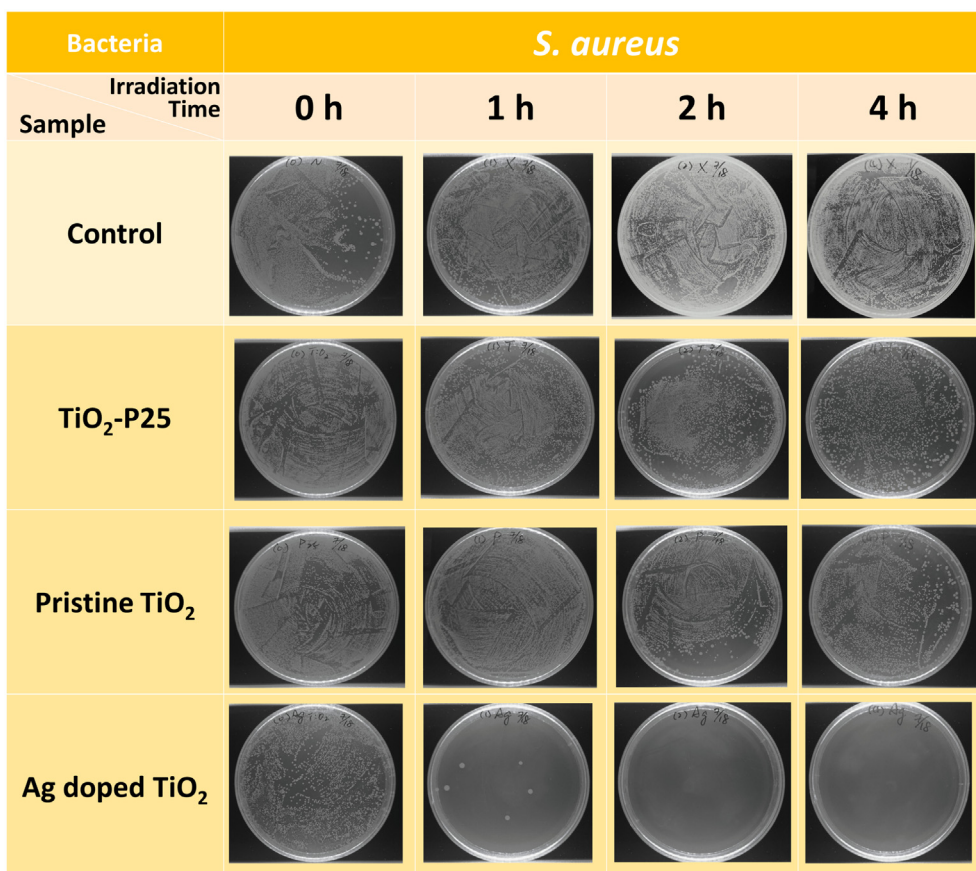


Fig. 6. The growth colonies of *S. aureus* (control sample) and *S. aureus* mixed with TiO<sub>2</sub>-P25, pristine TiO<sub>2</sub>, and Ag doped TiO<sub>2</sub>, treated with various visible light irradiation time and Ag doped TiO<sub>2</sub> inhibited *S. aureus* entirely since the first hour.

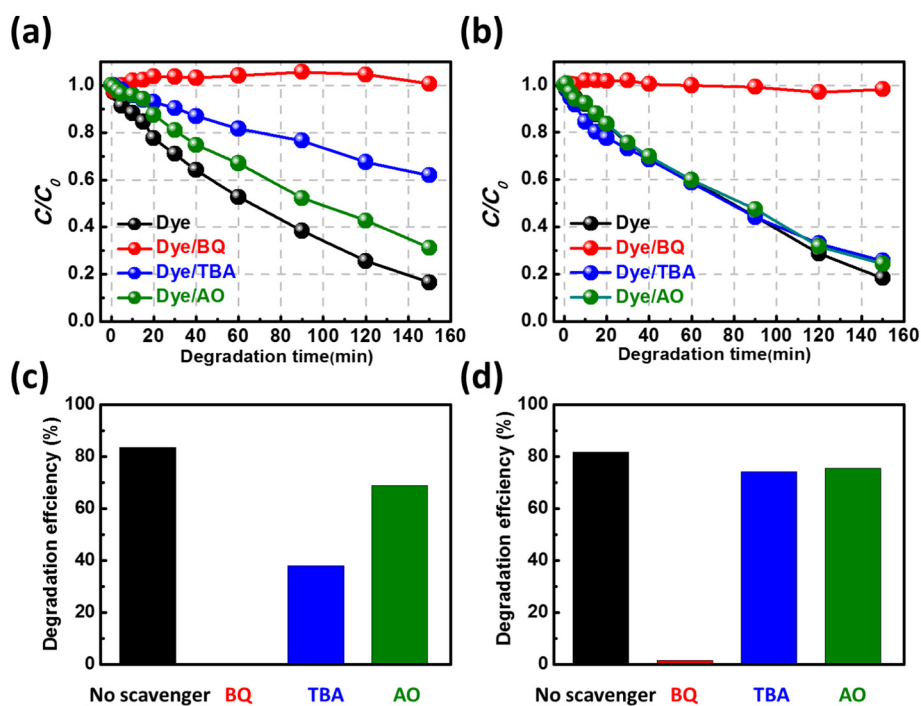


Fig. 7. The photodegradation charts of (a) pristine TiO<sub>2</sub> and (b) Ag doped TiO<sub>2</sub> toward the methyl orange under light irradiation, and their related degradation efficiency of (c) pristine TiO<sub>2</sub> and (d) Ag doped TiO<sub>2</sub>.

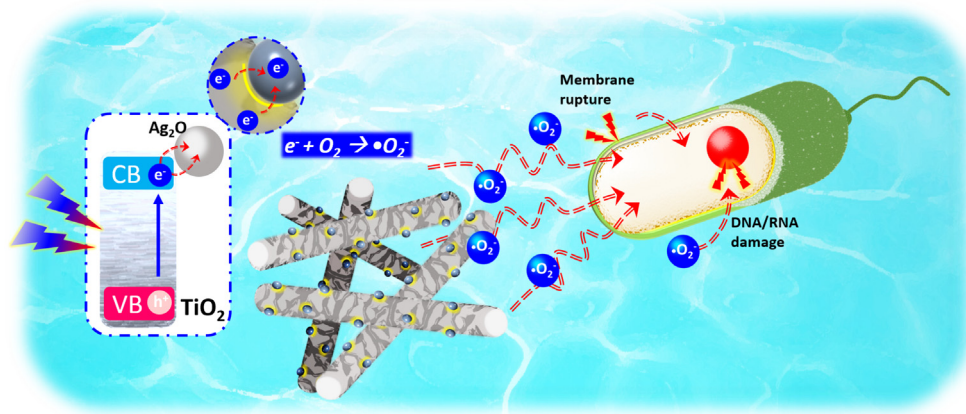


Fig. 8. The disinfection mechanism of Ag doped TiO<sub>2</sub> NFs.

in the pristine TiO<sub>2</sub> photodegradation. In contrast, there was a dramatic inhibition of photodegradation for Ag doped TiO<sub>2</sub> which is shown in Fig. 7(b). We observed that as BQ was added to the methyl orange solution, the decoloration behavior was extremely suppressed. With other scavengers, the efficiency was obscurely lessened (Fig. 7(d)). According to these decoloration behaviors and the results of degradation efficiency, Ag doped TiO<sub>2</sub> prefers to produce much more O<sub>2</sub><sup>•−</sup> radicals rather than other ROS. In summary, O<sub>2</sub><sup>•−</sup> radicals were the most dominant in the photodegradation for Ag doped TiO<sub>2</sub>. Meanwhile, these results indirectly proved that O<sub>2</sub><sup>•−</sup> radicals primarily contribute to the effective antibiotic property of Ag doped TiO<sub>2</sub>.

The possible disinfection mechanism of Ag doped TiO<sub>2</sub> NFs is shown in the following scheme in Fig. 8. When as-synthesized Ag doped TiO<sub>2</sub> NFs is irradiated by the incident light, the photoinduced electron-hole pairs form and electrons transit to conduction band in the meantime. As the charge carriers drift to surface effectively, they further transfer to Ag<sub>2</sub>O due to the lower conduction band and higher valence band of Ag<sub>2</sub>O [69–71]. The holes transfer to Ag<sub>2</sub>O, but do not produce the hydroxyl radicals owing to the unsuitable band alignment toward redox potential. For the electrons migration, the present metallic silver induced the Schottky barrier on the interface of Ag and Ag<sub>2</sub>O. The electrons pass through the junction as well as might be rectified to Ag from Ag<sub>2</sub>O. Then, electrons probably react with oxygen and produce the O<sub>2</sub><sup>•−</sup> radicals. These radicals with highly oxidized activity might rupture the cell membrane as well as damage DNA/RNA of bacteria. Eventually, the damages lead to bactericidal process.

#### 4. Conclusion

Many metal precursors were doped into TiO<sub>2</sub> to enhance the photodegradation activity. For the photodegradation of methyl orange, 5.00 mol%-Ag doped TiO<sub>2</sub>-600 shows the highest photodegradation rate. It represents the typical metal-semiconductor heterostructure systems that could be widely developed for the applications in photodegradation of organic dyes. For intensity study of silver derivatives in Ag doped TiO<sub>2</sub>, the results of synchrotron X-ray spectra and the energy dispersive X-ray analysis were consistent and indicated that Ag<sub>2</sub>O was loaded onto Ag doped TiO<sub>2</sub> NFs surface. Besides, the XPS analysis revealed the Ag<sub>2</sub>O mainly existed on the surface, while others included the metallic silver and few amount of AgO. For the disinfection, 5.00 mol%-Ag doped TiO<sub>2</sub>-600 NFs also has the outstanding capability against *E. coli* and *S. aureus* due to the synergistic effect of Ag<sub>2</sub>O and photo-induced ROS formed by the TiO<sub>2</sub> photocatalyst. The synthesized 5.00 mol%-Ag doped TiO<sub>2</sub>-600 NFs makes large-scale and convenient fabrication possible, and it has tremendous practical potentials in the photodegradation of environmental pollution and disinfection behavior.

#### Acknowledgements

The authors appreciate Prof. Wei-Fang Su at National Taiwan University and Dr. Ming-Tao Lee at National Synchrotron Radiation Research Centre (BL-13A1) for useful discussion and suggestions. The financial support from Ministry of Science and Technology, Taiwan (Project No. 106-2221-E-182-057-MY3, 107-2119-M-002-012, and 106-2632-E-182-001), Chang Gung University (QZRPD181) and Chang Gung Memorial Hospital, Linkou (CMRPD2H0161 and BMRPC74) are highly appreciated.

#### Appendix A. Supplementary data

Supplementary data to this article can be found online at <https://doi.org/10.1016/j.apsusc.2019.04.028>.

#### References

- [1] Q. Tang, X. Meng, Z. Wang, J. Zhou, H. Tang, One-step electrospinning synthesis of TiO<sub>2</sub>/g-C<sub>3</sub>N<sub>4</sub> nanofibers with enhanced photocatalytic properties, *Appl. Surf. Sci.* 430 (2018) 253–262.
- [2] R. Hao, G. Wang, C. Jiang, H. Tang, Q. Xu, In situ hydrothermal synthesis of g-C<sub>3</sub>N<sub>4</sub>/TiO<sub>2</sub> heterojunction photocatalysts with high specific surface area for Rhodamine B degradation, *Appl. Surf. Sci.* 411 (2017) 400–410.
- [3] C.L. Bianchi, S. Gatto, C. Pirola, A. Naldoni, A. Di Michele, G. Cerrato, V. Crocellà, V. Capucci, Photocatalytic degradation of acetone, acetaldehyde and toluene in gas-phase: comparison between nano and micro-sized TiO<sub>2</sub>, *Appl. Catal. B-Environ.* 146 (2014) 123–130.
- [4] A. Abdal-Hay, A.S.H. Makhlof, K.A. Khalil, Novel, facile, single-step technique of polymer/TiO<sub>2</sub> nanofiber composites membrane for photodegradation of methylene blue, *ACS Appl. Mater. Interfaces* 7 (2015) 13329–13341.
- [5] L. Korosi, B. Bogнар, M. Horvath, G. Schneider, J. Kovacs, A. Scarpellini, A. Castelli, M. Colombo, M. Prato, Hydrothermal evolution of PF-co-doped TiO<sub>2</sub> nanoparticles and their antibacterial activity against carbapenem-resistant *Klebsiella pneumoniae*, *Appl. Catal. B-Environ.* 231 (2018) 115–122.
- [6] C.M. Babu, R. Vinodh, B. Sundaravel, A. Abidov, M.M. Peng, W.S. Cha, H.-T. Jang, Characterization of reduced graphene oxide supported mesoporous Fe<sub>2</sub>O<sub>3</sub>/TiO<sub>2</sub> nanoparticles and adsorption of As(III) and As(V) from potable water, *J. Taiwan Inst. Chem. Eng.* 62 (2016) 199–208.
- [7] K. Qi, B. Cheng, J. Yu, W. Ho, Review on the improvement of the photocatalytic and antibacterial activities of ZnO, *J. Alloys Compd.* 727 (2017) 792–820.
- [8] S. Banerjee, D.D. Dionysiou, S.C. Pillai, Self-cleaning applications of TiO<sub>2</sub> by photo-induced hydrophilicity and photocatalysis, *Appl. Catal. B-Environ.* 176–177 (2015) 396–428.
- [9] C. Liu, T. Sun, L. Wu, J. Liang, Q. Huang, J. Chen, W. Hou, N-doped Na<sub>2</sub>Ti<sub>6</sub>O<sub>13</sub>@TiO<sub>2</sub> core-shell nanobelts with exposed {101} anatase facets and enhanced visible light photocatalytic performance, *Appl. Catal. B-Environ.* 170–171 (2015) 17–24.
- [10] S. Sorcar, Y. Hwang, C.A. Grimes, S.-I. In, Highly enhanced and stable activity of defect-induced titania nanoparticles for solar light-driven CO<sub>2</sub> reduction into CH<sub>4</sub>, *Mater. Today* 20 (2017) 507–515.
- [11] M.C. Wu, G. Toth, A. Sapi, A.R. Leino, Z. Konya, A. Kukovecz, W.F. Su, K. Kordas, Synthesis and photocatalytic performance of titanium dioxide nanofibers and the fabrication of flexible composite films from nanofibers, *J. Nanosci. Nanotechnol.* 12 (2012) 1421–1424.
- [12] S. Zhu, X. Xie, S.-C. Chen, S. Tong, G. Lu, D.Y.H. Pui, J. Sun, Cu-Ni nanowire-based

- TiO<sub>2</sub> hybrid for the dynamic photodegradation of acetaldehyde gas pollutant under visible light, *Appl. Surf. Sci.* 408 (2017) 117–124.
- [13] M.-C. Wu, P.-Y. Wu, T.-H. Lin, T.-F. Lin, Photocatalytic performance of Cu-doped TiO<sub>2</sub> nanofibers treated by the hydrothermal synthesis and air-thermal treatment, *Appl. Surf. Sci.* 430 (2018) 390–398.
- [14] L. Zhu, L. Gu, Y. Zhou, S. Cao, X. Cao, Direct production of a free-standing titanate and titania nanofiber membrane with selective permeability and cleaning performance, *J. Mater. Chem.* 21 (2011) 12503–12510.
- [15] G. Zhou, Y. Zhao, C. Zu, A. Manthiram, Free-standing TiO<sub>2</sub> nanowire-embedded graphene hybrid membrane for advanced Li/dissolved polysulfide batteries, *Nano Energy* 12 (2015) 240–249.
- [16] M. Ghosh, J. Liu, S.S.C. Chuang, S.C. Jana, Fabrication of hierarchical V<sub>2</sub>O<sub>5</sub> nanorods on TiO<sub>2</sub> nanofibers and their enhanced photocatalytic activity under visible light, *ChemCatChem* 10 (2018) 3305–3318.
- [17] R. Shi, Z. Li, H. Yu, L. Shang, C. Zhou, G.I.N. Waterhouse, L.-Z. Wu, T. Zhang, Effect of nitrogen doping level on the performance of N-doped carbon quantum dot/TiO<sub>2</sub> composites for photocatalytic hydrogen evolution, *ChemSusChem* 10 (2017) 4650–4656.
- [18] C.-W. Hsu, C.-H. Li, L. Zhang, S.-Y. Lu, N-doped carbon dots@layer facilitated heterostructure of TiO<sub>2</sub> polymorphs for efficient photoelectrochemical water oxidation, *J. Taiwan Inst. Chem. Eng.* 93 (2018) 388–396.
- [19] P. Wang, G. Yin, Q. Bi, X. Huang, X. Du, W. Zhao, F. Huang, Efficient photocatalytic reduction of CO<sub>2</sub> using carbon-doped amorphous titanium oxide, *ChemCatChem* 10 (2018) 3854–3861.
- [20] M.C. Wu, J. Hiltunen, A. Sapi, A. Avila, W. Larsson, H.C. Liao, M. Huuhtanen, G. Toth, A. Shchukarev, N. Laufer, A. Kukovec, Z. Konya, J.P. Mikkola, R. Keiski, W.F. Su, Y.F. Chen, H. Jantunen, P.M. Ajayan, R. Vajtai, K. Kordas, Nitrogen-doped anatase nanofibers decorated with noble metal nanoparticles for photocatalytic production of hydrogen, *ACS Nano* 5 (2011) 5025–5030.
- [21] M.S. Akple, J. Low, S. Liu, B. Cheng, J. Yu, W. Ho, Fabrication and enhanced CO<sub>2</sub> reduction performance of N-self-doped TiO<sub>2</sub> microsheet photocatalyst by bi-cocatalyst modification, *J. CO<sub>2</sub> Util.* 16 (2016) 442–449.
- [22] M.S. Akple, J. Low, Z. Qin, S. Wageh, A.A. Al-Ghamdi, J. Yu, S. Liu, Nitrogen-doped TiO<sub>2</sub> microspheres with enhanced visible light photocatalytic activity for CO<sub>2</sub> reduction, *Chin. J. Catal.* 36 (2015) 2127–2134.
- [23] M. Zhu, C. Zhai, L. Qiu, C. Lu, A.S. Paton, Y. Du, M.C. Goh, New method to synthesize S-doped TiO<sub>2</sub> with stable and highly efficient photocatalytic performance under indoor sunlight irradiation, *ACS Sustainable Chem. Eng.* 3 (2015) 3123–3129.
- [24] L.G. Devi, R. Kavitha, Enhanced photocatalytic activity of sulfur doped TiO<sub>2</sub> for the decomposition of phenol: a new insight into the bulk and surface modification, *Mater. Chem. Phys.* 143 (2014) 1300–1308.
- [25] P. Zhang, T. Tachikawa, M. Fujitsuka, T. Majima, In situ fluorine doping of TiO<sub>2</sub> superstructures for efficient visible-light driven hydrogen generation, *ChemSusChem* 9 (2016) 617–623.
- [26] W. Yu, X. Liu, L. Pan, J. Li, J. Liu, J. Zhang, P. Li, C. Chen, Z. Sun, Enhanced visible light photocatalytic degradation of methylene blue by F-doped TiO<sub>2</sub>, *Appl. Surf. Sci.* 319 (2014) 107–112.
- [27] G. Veréb, L. Manczinger, A. Oszkó, A. Sienkiewicz, L. Forró, K. Mogyorósi, A. Dombi, K. Hernádi, Highly efficient bacteria inactivation and phenol degradation by visible light irradiated iodine doped TiO<sub>2</sub>, *Appl. Catal. B-Environ.* 129 (2013) 194–201.
- [28] Q. Zhang, Y. Li, E.A. Ackerman, M. Gajdardziska-Josifovska, H. Li, Visible light responsive iodine-doped TiO<sub>2</sub> for photocatalytic reduction of CO<sub>2</sub> to fuels, *Appl. Catal., A* 400 (2011) 195–202.
- [29] Y. Lu, X. Zhang, Y. Chu, H. Yu, M. Huo, J. Qu, J.C. Crittenden, H. Huo, X. Yuan, Cu<sub>2</sub>O nanocrystals/TiO<sub>2</sub> microspheres film on a rotating disk containing long-afterglow phosphor for enhanced round-the-clock photocatalysis, *Appl. Catal. B-Environ.* 224 (2018) 239–248.
- [30] V.B. Koli, S. Mavengere, J.-S. Kim, Boron-doped TiO<sub>2</sub>-CNTs nanocomposites for photocatalytic application, *J. Mater. Sci. Mater. Electron.* 29 (2018) 16660–16672.
- [31] M. Szkoda, A. Lisowska-Oleksiak, K. Siuzdak, Optimization of boron-doping process of titania nanotubes via electrochemical method toward enhanced photoactivity, *J. Solid State Electrochem.* 20 (2016) 1765–1774.
- [32] L.G. Devi, R. Kavitha, A review on non metal ion doped titania for the photocatalytic degradation of organic pollutants under UV/solar light: role of photo-generated charge carrier dynamics in enhancing the activity, *Appl. Catal. B-Environ.* 140 (2013) 559–587.
- [33] J. Low, B. Cheng, J. Yu, Surface modification and enhanced photocatalytic CO<sub>2</sub> reduction performance of TiO<sub>2</sub>: a review, *Appl. Surf. Sci.* 392 (2017) 658–686.
- [34] S. Veziroglu, M.Z. Ghori, M. Kamp, L. Kienle, H.-G. Rubahn, T. Strunskus, J. Fiutowski, J. Adam, F. Faupel, O.C. Aktas, Photocatalytic growth of hierarchical Au needle clusters on highly active TiO<sub>2</sub> thin film, *Adv. Mater. Interfaces* 5 (2018) 1800465.
- [35] Z.H.N. Al-Azri, W.-T. Chen, A. Chan, V. Jovic, T. Ina, H. Idriss, G.I.N. Waterhouse, The roles of metal co-catalysts and reaction media in photocatalytic hydrogen production: performance evaluation of M/TiO<sub>2</sub> photocatalysts (M=Pd, Pt, Au) in different alcohol–water mixtures, *J. Catal.* 329 (2015) 355–367.
- [36] M. Murdoch, G.I.N. Waterhouse, M.A. Nadeem, J.B. Metson, M.A. Keane, R.F. Howe, J. Llorca, H. Idriss, The effect of gold loading and particle size on photocatalytic hydrogen production from ethanol over Au/TiO<sub>2</sub> nanoparticles, *Nat. Chem.* 3 (2011) 489.
- [37] S.A.H. Jalali, A.R. Allafchian, S.S. Banifatem, I. Ashrafi Tamai, The antibacterial properties of Ag/TiO<sub>2</sub> nanoparticles embedded in silane sol–gel matrix, *J. Taiwan Inst. Chem. Eng.* 66 (2016) 357–362.
- [38] W. Chen, Y. Wang, S. Liu, L. Gao, L. Mao, Z. Fan, W. Shanguan, Z. Jiang, Non-noble metal Cu as a cocatalyst on TiO<sub>2</sub> nanorod for highly efficient photocatalytic hydrogen production, *Appl. Surf. Sci.* 445 (2018) 527–534.
- [39] M.-C. Wu, P.-Y. Wu, T.-H. Lin, T.-F. Lin, Photocatalytic performance of Cu-doped TiO<sub>2</sub> nanofibers treated by the hydrothermal synthesis and air-thermal treatment, *Appl. Surf. Sci.* 430 (2018) 390–398.
- [40] N. Smirnova, I. Petrik, V. Vorobets, G. Kolbasov, A. Eremenko, Sol-gel synthesis, photo- and electrocatalytic properties of mesoporous TiO<sub>2</sub> modified with transition metal ions, *Nanoscale Res. Lett.* 12 (2017) 239.
- [41] M. Crişan, D. Mardare, A. Ianculescu, N. Drăgan, I. Niţoi, D. Crişan, M. Voicescu, L. Todan, P. Oancea, C. Adomniţei, M. Dobromir, M. Gabrovsk, B. Vasile, Iron doped TiO<sub>2</sub> films and their photoactivity in nitrobenzene removal from water, *Appl. Surf. Sci.* 455 (2018) 201–215.
- [42] S. Sood, A. Umar, S.K. Mehta, S.K. Kansal, Highly effective Fe-doped TiO<sub>2</sub> nanoparticles photocatalysts for visible-light driven photocatalytic degradation of toxic organic compounds, *J. Colloid Interface Sci.* 450 (2015) 213–223.
- [43] Z. Zhu, R.-J. Wu, The degradation of formaldehyde using a Pt@TiO<sub>2</sub> nanoparticles in presence of visible light irradiation at room temperature, *J. Taiwan Inst. Chem. Eng.* 50 (2015) 276–281.
- [44] M.-Y. Xie, K.-Y. Su, X.-Y. Peng, R.-J. Wu, M. Chavali, W.-C. Chang, Hydrogen production by photocatalytic water-splitting on Pt-doped TiO<sub>2</sub>-ZnO under visible light, *J. Taiwan Inst. Chem. Eng.* 70 (2017) 161–167.
- [45] M.-C. Wu, W.-K. Huang, T.-H. Lin, Y.-J. Lu, Photocatalytic hydrogen production and photodegradation of organic dyes of hydrogenated TiO<sub>2</sub> nanofibers decorated metal nanoparticles, *Appl. Surf. Sci.* 469 (2019) 34–43.
- [46] M. Długocka, J. Luczak, Ż. Polkowska, A. Zaleska-Medynska, The effect of microemulsion composition on the morphology of Pd nanoparticles deposited at the surface of TiO<sub>2</sub> and photoactivity of Pd-TiO<sub>2</sub>, *Appl. Surf. Sci.* 405 (2017) 220–230.
- [47] N.u. Saqib, R. Adnan, I. Shah, A mini-review on rare earth metal-doped TiO<sub>2</sub> for photocatalytic remediation of wastewater, *Environ. Sci. Pollut. Res.* 23 (2016) 15941–15951.
- [48] G. Rossi, L. Pasquini, D. Catone, A. Piccioni, N. Patelli, A. Paladini, A. Molinari, S. Caramori, P. O’Keeffe, F. Boscherini, Charge carrier dynamics and visible light photocatalysis in vanadium-doped TiO<sub>2</sub> nanoparticles, *Appl. Catal. B-Environ.* 237 (2018) 603–612.
- [49] D.V. Aware, S.S. Jadhav, Synthesis, characterization and photocatalytic applications of Zn-doped TiO<sub>2</sub> nanoparticles by sol–gel method, *Appl. Nanosci.* 6 (2016) 965–972.
- [50] S. Pang, J.-G. Huang, Y. Su, B. Geng, S.-Y. Lei, Y.-T. Huang, C. Lyu, X.-J. Liu, Synthesis and modification of Zn-doped TiO<sub>2</sub> nanoparticles for the photocatalytic degradation of tetracycline, *Photochem. Photobiol.* 92 (2016) 651–657.
- [51] J. Choi, H. Park, M.R. Hoffmann, Effects of single metal-ion doping on the visible-light photoreactivity of TiO<sub>2</sub>, *J. Phys. Chem. C* 114 (2010) 783–792.
- [52] S.-Y. Ryu, J.W. Chung, S.-Y. Kwak, Dependence of photocatalytic and antimicrobial activity of electrospun polymeric nanofiber composites on the positioning of Ag–TiO<sub>2</sub> nanoparticles, *Compos. Sci. Technol.* 117 (2015) 9–17.
- [53] M. Li, Z. Xing, J. Jiang, Z. Li, J. Yin, J. Kuang, S. Tan, Q. Zhu, W. Zhou, Surface plasmon resonance-enhanced visible-light-driven photocatalysis by Ag nanoparticles decorated S-TiO<sub>2-x</sub> nanorods, *J. Taiwan Inst. Chem. Eng.* 82 (2018) 198–204.
- [54] T.K. Rahul, N. Sandhyarani, Plasmonic and photonic effects on hydrogen evolution over chemically modified titania inverse opals, *ChemNanoMat* 4 (2018) 642–648.
- [55] J. Low, S. Qiu, D. Xu, C. Jiang, B. Cheng, Direct evidence and enhancement of surface plasmon resonance effect on Ag-loaded TiO<sub>2</sub> nanotube arrays for photocatalytic CO<sub>2</sub> reduction, *Appl. Surf. Sci.* 434 (2018) 423–432.
- [56] P. Ganguly, C. Byrne, A. Breen, S.C. Pillai, Antimicrobial activity of photocatalysts: fundamentals, mechanisms, kinetics and recent advances, *Appl. Catal. B-Environ.* 225 (2018) 51–75.
- [57] Y. Li, W. Zhang, J. Niu, Y. Chen, Mechanism of photogenerated reactive oxygen species and correlation with the antibacterial properties of engineered metal-oxide nanoparticles, *ACS Nano* 6 (2012) 5164–5173.
- [58] X. Yang, J. Qin, Y. Jiang, K. Chen, X. Yan, D. Zhang, R. Li, H. Tang, Fabrication of P25/Ag<sub>3</sub>PO<sub>4</sub>/graphene oxide heterostructures for enhanced solar photocatalytic degradation of organic pollutants and bacteria, *Appl. Catal. B-Environ.* 166–167 (2015) 231–240.
- [59] S. Chen, Y. Guo, H. Zhong, S. Chen, J. Li, Z. Ge, J. Tang, Synergistic antibacterial mechanism and coating application of copper/titanium dioxide nanoparticles, *Chem. Eng. J.* 256 (2014) 238–246.
- [60] S. Yao, X. Feng, J. Lu, Y. Zheng, X. Wang, A.A. Volinsky, L.-N. Wang, Antibacterial activity and inflammation inhibition of ZnO nanoparticles embedded TiO<sub>2</sub> nanotubes, *Nanotechnology* 29 (2018) 244003.
- [61] X. Zhang, M. Li, X. He, R. Hang, X. Huang, Y. Wang, X. Yao, B. Tang, Antibacterial activity of single crystalline silver-doped anatase TiO<sub>2</sub> nanowire arrays, *Appl. Surf. Sci.* 372 (2016) 139–144.
- [62] M.-C. Wu, P.-H. Lee, D.-L. Lee, Enhanced photocatalytic activity of palladium decorated TiO<sub>2</sub> nanofibers containing anatase-rutile mixed phase, *Int. J. Hydrog. Energy* 40 (2015) 4558–4566.
- [63] M.-C. Wu, A. Sapi, A. Avila, M. Szabó, J. Hiltunen, M. Huuhtanen, G. Tóth, Á. Kukovec, Z. Konya, R. Keiski, W.-F. Su, H. Jantunen, K. Kordas, Enhanced photocatalytic activity of TiO<sub>2</sub> nanofibers and their flexible composite films: decomposition of organic dyes and efficient H<sub>2</sub> generation from ethanol–water mixtures, *Nano Res.* 4 (2011) 360–369.
- [64] A. Katti, S.R. Venna, M.A. Carreon, Self-assembly hydrothermal assisted synthesis of mesoporous anatase in the presence of ethylene glycol, *Catal. Commun.* 10 (2009) 2036–2040.
- [65] Q.L. Feng, J. Wu, G.Q. Chen, F.Z. Cui, T.N. Kim, J.O. Kim, A mechanistic study of the antibacterial effect of silver ions on *Escherichia coli* and *Staphylococcus aureus*, *J. Biomed. Mater. Res.* 52 (2000) 662–668.

- [66] W.K. Jung, H.C. Koo, K.W. Kim, S. Shin, S.H. Kim, Y.H. Park, Antibacterial activity and mechanism of action of the silver ion in *Staphylococcus aureus* and *Escherichia coli*, *Appl. Environ. Microbiol.* 74 (2008) 2171–2178.
- [67] W.R. Li, X.B. Xie, Q.S. Shi, H.Y. Zeng, Y.S. Ou-Yang, Y.B. Chen, Antibacterial activity and mechanism of silver nanoparticles on *Escherichia coli*, *Appl. Microbiol. Biotechnol.* 85 (2010) 1115–1122.
- [68] T.C. Dakal, A. Kumar, R.S. Majumdar, V. Yadav, Mechanistic basis of antimicrobial actions of silver nanoparticles, *Front. Microbiol.* 7 (2016) 1831.
- [69] B. Liu, L. Mu, B. Han, J. Zhang, H. Shi, Fabrication of  $\text{TiO}_2/\text{Ag}_2\text{O}$  heterostructure with enhanced photocatalytic and antibacterial activities under visible light irradiation, *Appl. Surf. Sci.* 396 (2017) 1596–1603.
- [70] H.-T. Ren, Q. Yang, Fabrication of  $\text{Ag}_2\text{O}/\text{TiO}_2$  with enhanced photocatalytic performances for dye pollutants degradation by a pH-induced method, *Appl. Surf. Sci.* 396 (2017) 530–538.
- [71] M. Zou, H. Liu, L. Feng, F. Xiong, T. Thomas, M. Yang, Effect of nitridation on visible light photocatalytic behavior of microporous (Ag,  $\text{Ag}_2\text{O}$ ) co-loaded  $\text{TiO}_2$ , *Microporous Mesoporous Mater.* 240 (2017) 137–144.